From clouds to comets: tracing the molecular journey of interstellar ices in the JWST era

Slavicinska, K.

5

Laboratory infrared spectra and band strengths of carbonyl sulfide (OCS) in CH_3OH- and CO-rich ice mixtures for analyzing interstellar ice observations

Katerina Slavicinska, Charlotte Coone, Bryce Benz, Harold Linnartz, A. C. Adwin Boogert, Ko-Ju Chuang

ACS Earth & Space Chemistry (2025), 9(8), 2148-2158

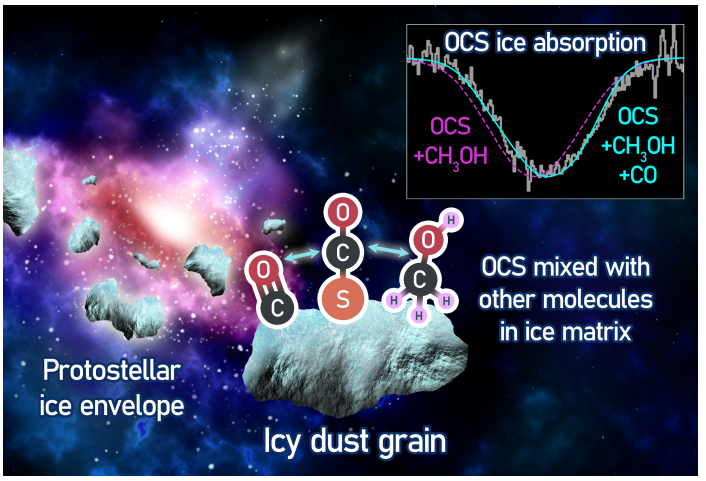

Abstract

Carbonyl sulfide (OCS) is currently the only securely detected sulfur-bearing species in interstellar ices, making it an ideal window into the solid-state sulfur chemistry in dense star-forming regions. Previous astronomical observations of the OCS asymmetric stretching mode (ν_3) at $\sim$2040 cm^{-1} ($\sim$4.9 μm) demonstrate that interstellar OCS may be embedded in CH_3OH-rich ices, indicating that OCS likely forms in the coldest, densest parts of star-forming regions where catastrophic CO freezeout occurs. However, a significant portion of OCS ice observations cannot be fit with binary OCS:CH_3OH laboratory ice mixtures alone, suggesting a greater degree of chemical complexity in the local ice environment. With this work, we aim to aid future studies of the abundance, physicochemical environment, and evolutionary history of interstellar OCS ice, now enabled for many more interstellar environments by the *James Webb* Space Telescope. We provide a library of new laboratory IR transmission spectra of OCS in CH_3OH- and CO-rich ice mixtures, some of which also include H_2S and H_2O. Of these new spectra, the tertiary OCS:CO:CH_3OH ice mixtures provide the best fits to observations of high-mass protostars, providing further support for the hypothesis that OCS forms with CH_3OH, possibly via chemical pathways involving frozen-out CO. We calculate apparent band strengths of the OCS ν_3 mode in OCS:CH_3OH and OCS:CO:CH_3OH ice mixtures. The derived values are consistent (within uncertainties) with the apparent band strength of the feature in pure OCS ice, 1.2×10^{-16} cm molec^{-1}. We therefore recommend using this value when quantifying interstellar OCS ice column densities.

5.1 Introduction

In the past two decades, sulfur-bearing ices have been a major focus of astrochemical research due to the observed gas-phase sulfur depletion in dense star-forming regions (Jiménez-Escobar & Muñoz Caro 2011; Chen et al. 2014; Hudson & Gerakines 2018; Vidal & Wakelam 2018; Laas & Caselli 2019). However, of the many sulfur-bearing molecules proposed by such

works to exist in interstellar ices, carbonyl sulfide (OCS) remains the only secure detection despite its low abundance (∼0.05-0.5% with respect to H_2O, Boogert et al. 2022; McClure et al. 2023). This is due to the high band strength (on the order of 10^{-16} cm molec^{-1}, Yarnall & Hudson 2022) and the relatively isolated peak position (4.9 μm) of its strongest IR vibrational feature, the asymmetric stretching mode (ν_3). These spectral properties aided its early first detection (Geballe et al. 1985) and subsequent identification as OCS (Palumbo et al. 1995) in ground-based IR spectra of the ice envelope surrounding the massive protostar W33A. Since then, OCS has been detected toward the ice envelopes of over 20 massive protostars (Palumbo et al. 1997; Gibb et al. 2004; Boogert et al. 2022; Tyagi et al. 2025), as well as the ice envelope of one low-mass protostar (Aikawa et al. 2012) and two background stars behind a dense molecular cloud (McClure et al. 2023).

Although OCS is decidedly not a major sulfur carrier in dense star-forming regions, its strong ν_3 absorption feature offers a unique window into the solid-state sulfur chemistry of such environments. Experiments presented in Palumbo et al. 1995 demonstrated that the profile of this band is highly dependent on the chemical composition of the surrounding ice matrix, and out of all the laboratory ice mixtures compared to the observations, the ices rich in CH_3OH provided the best fit to many of the observed absorptions (Palumbo et al. 1997; Boogert et al. 2022). Additionally, in a survey of 23 massive protostars, Boogert et al. 2022 found that OCS ice column densities correlate well with the ice column densities of CH_3OH, OCN^-, and the polar CO component, while they correlate poorly with the ice column densities of H_2O and the apolar CO component. A correlation between OCS and CH_3OH column densities (i.e., small scatter in the OCS/CH_3OH ratio) is also observed toward massive protostars in the gas phase (Santos et al. 2024b). These results indicate that most OCS ice likely formed alongside CH_3OH after the heavy CO freezeout stage, in the densest regions of the clouds and envelopes, possibly via routes such as the sulfurization of CO (Shingledecker et al. 2020) or the addition of SH radicals to CO (Santos et al. 2024a).

Despite these indications that interstellar OCS ice may be embedded in a CH_3OH-rich environment, the band strength of the OCS ν_3 feature in CH_3OH-rich ices has not been measured. So far, most currently reported interstellar OCS ice column densities (Palumbo et al. 1997; Boogert et al. 2022) were calculated using an OCS ν_3 band strength of 1.5×10^{-16} cm molec^{-1}, derived for pure OCS ice using a refractive index measured for liquid OCS and a simply assumed ice density of 1 g cm^{-3} (Hudgins et al. 1993). Recently, Yarnall & Hudson 2022 published an improved OCS ν_3 band strength of 1.2×10^{-16} cm molec^{-1} for both pure OCS ice and OCS in a 1:20 binary mixture with H_2O ice using new refractive index and density values that were measured directly for amorphous OCS ice. Nevertheless, existing OCS observations indicate that neither pure nor H_2O-dominated OCS ices are relevant to the interstellar medium.

Furthermore, the large sample of OCS ice observations in Boogert et al. 2022 revealed that in a significant portion of the investigated sources, the observed OCS ν_3 peak position is slightly redshifted (by up to ∼0.01 μm) relative to the peak positions of OCS in binary laboratory ice mixtures with CH_3OH. In contrast, comparably redshifted peak positions of the OCS feature are observed in laboratory spectra of CO- and H_2S-containing ices that were irradiated and then heated (Ferrante et al. 2008; Garozzo et al. 2010). Thus, the observed redshifts may indicate a higher degree of chemical complexity in the ice matrix in which OCS is embedded and could be interpreted as tentative, indirect evidence for OCS formation via energetic processing of other sulfur-bearing ices. However, a lack of publicly available laboratory IR

spectra of OCS in more chemically complex ice matrices with carefully controlled ice mixing ratios precludes drawing more specific conclusions about the chemical environment of OCS toward these sources with redshifted OCS features.

The present work aims to fill several gaps in experimental OCS ice studies. First, we present the transmission IR spectrum from 4000-500 cm^{-1} (2.5-20 μm) of both amorphous and crystalline OCS ice and calculate the band strengths of all of its fundamental vibrational modes using the most recently measured refractive index and density of amorphous OCS ice (Yarnall & Hudson 2022). Then, we aim to aid deeper investigations into the chemical environment of interstellar OCS ice molecules by providing laboratory IR spectra of OCS in more chemically complex, tertiary ice mixtures with a focus on mixtures rich in CH_3OH and CO, given their aforementioned plausible physicochemical links to OCS, and because interstellar CH_3OH ice is thought to form primarily via CO hydrogenation after catastrophic CO freezeout (Watanabe & Kouchi 2002; Fuchs et al. 2009), so it is expected and observationally supported (Cuppen et al. 2011; Penteado et al. 2015) that CO and CH_3OH will be mixed in interstellar ices to some degree. Some of the investigated mixtures also include H_2S, a suggested chemical precursor of OCS (Ferrante et al. 2008; Santos et al. 2024a), and H_2O, the most abundant observable interstellar ice (Boogert et al. 2015). We also provide updated IR spectra of binary OCS ice mixtures using modern ice co-deposition methodologies that result in more accurate and controlled ice mixing ratios (Yarnall & Hudson 2022). We report the peak positions, FWHMs, and relative integrated absorbances of the OCS ν_3 modes observed in these mixtures at temperatures spanning from 15-100 K to facilitate future analyses of astronomically observed OCS ice profiles. The spectral data are made publicly available on the Leiden Ice Database (LIDA, Rocha et al. 2022). Finally, we compare our updated database of OCS ice data to previous OCS ice observations to determine which of our mixtures are most likely to be analogous to the chemical environment of OCS in interstellar ices and calculate the apparent band strengths of the OCS ν_3 mode in these mixtures. This set of experimental data can be used by the community to improve the understanding of the abundance, physicochemical environment, and evolutionary history of interstellar OCS ice in an era of copious new ice observations in environments like cold dark clouds, the faintest and youngest low-mass protostars, and extragalactic star-forming regions that have been enabled by the recently launched *James Webb* Space Telescope.

5.2 Methods

5.2.1 Experimental setup

All of the data presented in this work were collected using the Infrared Absorption Setup for Ice Spectroscopy (IRASIS) at the Leiden Laboratory for Astrophysics. A schematic of the setup is presented by Rachid et al. 2021, and subsequent upgrades are described by Slavicinska et al. 2023. To briefly summarize, the setup consists of an ultrahigh vacuum chamber (ultimate pressure $<1\times10^{-9}$ mbar) containing a KBr substrate that can be cooled down to 15 K with a closed-cycle He cryostat. Three independent dosing lines with independent gas reservoirs, leak valves, and chamber inlets located at the bottom of the chamber enable background vapor deposition of ices on the cryo-cooled substrate. The deposition of these ices can be monitored on both sides of the substrate via laser interferometry with two 633 nm HeNe

laser beams positioned at 45° relative to the substrate normal, as well as via transmission IR spectroscopy with an FTIR beam positioned at 0° relative to the substrate normal. Ices are typically deposited to thicknesses on the order of hundreds to thousands of monolayers (depending on what thickness is needed to achieve satisfactory S/N of the ice feature of interest). The sample temperature can be kept constant or changed at a set rate via proportional-integral-derivative control. Gaseous species present in the chamber during deposition or warm-up are monitored with a quadrupole mass spectrometer (QMS).

In the experiments presented in this work, deposition pressures ranged from the order of 10^{-8} mbar in the case of the pure OCS ices to the order of 10^{-6} mbar in the case of the most diluted OCS ice mixtures. Deposition timescales ranged from ∼20-50 min. The IR spectra presented in this work were collected from 4000-500 cm^{-1} (2.5-20 μm) with a spectral resolution of 0.5 cm^{-1}. Each spectrum consists of 128 averaged scans collected over a period of ∼3.5 min. During the warm-ups, the substrate was heated at a rate of 25 K h^{-1}, resulting in ∼1.5 K intervals between the spectra collected during warm-up.

The liquids and gases used in this work include carbonyl sulfide (Linde Gas, ≥99.9%), methanol (Sigma Aldrich, ≥99.9%), carbon monoxide (Linde Gas, ≥99.997%), water (Milli-Q, Type I), and hydrogen sulfide (Linde Gas, ≥99.5%).

5.2.2 Mixing ratio calibration

This work uses similar methods to those described by Yarnall & Hudson 2022 and Slavicinska et al. 2023 to create binary and tertiary ice mixtures with specific ice component ratios. The position of each leak valve is independently calibrated to output the desired deposition rate of each ice component. This is achieved by first depositing each species of interest in pure form at 15 K and simultaneously monitoring the laser interference pattern and the QMS signal of a selected mass peak of the species of interest throughout the deposition. The period of the laser interference pattern T during deposition can be converted to an ice column density growth rate dN/dt via the following equation:

$$\frac{dN}{dt} = \frac{\lambda}{2\sqrt{n^2 sin^2\theta}} \times \frac{\rho N_A}{MT} \tag{5.1}$$

where λ is the wavelength of the laser, n is the ice refractive index, θ is the laser angle of incidence, ρ is the ice density, N_A is Avogadro's number, and M is the ice molar mass. The literature n and ρ values used to obtain the ice column density growth rates of the species investigated in this work are presented in Table 5.1. The total errors on these growth rates stem from the uncertainties of the literature n and ρ values used, estimated here to be on the order of ∼5 and 15%, respectively, based on typical variations seen in these values between measurements made in different laboratories and with different setup configurations (Bouilloud et al. 2015; Loeffler et al. 2016; Luna et al. 2022). The variations in ice densities measured in different laboratories are often primarily due to different deposition methods resulting in different ice porosities in the case of amorphous ices (Loeffler et al. 2016), where background deposition (the method employed in this work) typically produces more porous ice than directional deposition (the method employed by, e.g., Yarnall & Hudson 2022), although the magnitude of variation depends on the particular species. Additionally, there is a ±5° uncertainty of the laser angle of incidence, which corresponds to an error of ∼4% in the ice growth rates. This propagates to a total uncertainty on the ice growth rate of 16%.

Table 5.1: Literature ice refractive index and density values of pure ices used to calculate ice column density growth rates in this work.

Species	n	ρ (g cm^{-3})	ref.
OCS	1.436	1.248	36
CH_3OH	1.257	0.636	20
CO	1.297	0.870	19
H_2O	1.234	0.719	36
H_2S	1.407	0.944	36

A calibration curve is then generated by repeating a pure ice deposition with at least five different growth rates and finding the best-fit correlation between the calculated ice column density growth rates and the average QMS signal of a selected mass peak throughout the deposition. For all of the investigated molecules, the correlation was well fit using a linear equation, with R^2 values ranging from 0.995-0.9998. Each leak valve can then be calibrated to a desired deposition rate of a specific species by filling the gas reservoir connected to that leak valve with a specific pressure of the gas or vapor of the species and then adjusting the leak valve until the QMS signal that corresponds to the desired ice column density growth rate in the calibration curve is reached. The exact deposition rate is ascertained by performing multiple laser interference control measurements of pure ice deposition rates using the calibrated leak valve position. Five of such measurements typically have a standard deviation of 0.3-3%, and their average varies by 2-5% from the desired growth rate used to calculate the corresponding QMS signal on the calibration curve. However, these experimental errors are negligible when compared to the uncertainty on the calculated ice growth rate caused by the estimated uncertainty of the literature ρ value.

After this calibration is complete for all of the desired ice components, an ice mixture with specific component ratios can be deposited. First, each gas reservoir is filled with the same pressure of the pure gas or vapor used during the leak valve calibration. During this step, deposition of the gases or vapors into the chamber via the opened leak valves is prevented via shut valves preceding the leak valves. Once all of the gas reservoirs have been filled, all of the shut valves are opened to begin simultaneous deposition. As mentioned by Yarnall & Hudson 2022, this method assumes that the ice column density growth rates during co-deposition remain the same as during the deposition of each component individually.

5.2.3 Apparent band strengths

For pure OCS ice, apparent band strengths were calculated by depositing six pure OCS ices at five different deposition rates (one deposition rate was repeated to check for consistency), with rates ranging from ∼0.2-2 μm h^{-1}. Throughout each deposition, transmission IR spectra of the growing ice sample were continuously collected. The changes in the integrated optical depths of the OCS features of interest over time $d\int \tau\, d\nu/dt$ were determined by finding the best linear fits to the integrated optical depths over time. High R^2 values of these fits in the case of the ν_3 feature (≥0.9996) indicate very uniform ice growth rates throughout all of the

depositions. The corresponding ice column density growth rate for each of these measurements was then determined using Equation 5.1 to convert the period of the laser interference pattern generated during each deposition to dN/dt.

The best linear fits to the six independent $d\int\tau\,d\nu/dt$ versus dN/dt measurements, plotted in time-derivative Beer's law plots, were then determined via the York method for fitting data with errors on both X and Y variables (York 1966). The slopes of these fits are reported as the apparent band strengths, A', of the pure OCS bands. Using the time derivatives of the ice column densities and integrated optical depths rather than the absolute values of these variables ensures that any residues from previous experiments present on the substrate do not contribute to the calculated ice column densities. It also eliminates errors caused by human imprecision in stopping deposition at a specific time or ice thickness. The error of the slope calculated by the York method yields A' uncertainties $\sim$10%, with the dominant source of uncertainty being the uncertainty of the ρ value used in Equation 5.1.

For OCS ice mixtures, apparent band strengths were only determined for the ν_3 mode, and they were calculated via a different method than the pure apparent band strengths, as the ice column density growth rates could not be determined from the laser intereference patterns since the n and ρ values of the ice mixtures are not known. Instead, the leak valve used to deposit OCS was calibrated to correspond to a specific OCS ice growth rate, and five pure OCS ice depositions were performed using this leak valve position. The same leak valve position was then used to dose OCS during the deposition of the ice mixture of interest. The apparent band strength of the OCS feature in each mixture was subsequently calculated using the equation:

$$A'_{mix} = A'_{pure} \times \frac{d\int\tau_{mix}\,d\nu/dt}{d\int\tau_{pure,avg}\,d\nu/dt} \tag{5.2}$$

where $d\int\tau_{mix}\,d\nu/dt$ is the change in integrated optical depth of the OCS ν_3 feature during the deposition of each mixture of interest, $d\int\tau_{pure,avg}\,d\nu/dt$ is the average change in integrated optical depth of the OCS ν_3 feature during the five pure OCS depositions (standard deviation = 0.8%), and A'_{pure} is the apparent band strength of the ν_3 mode of pure OCS.

5.3 Results

5.3.1 Pure OCS ice

The IR spectrum of pure OCS ice in both amorphous and crystalline forms is presented in Figure 5.1. The ν_3 (asymmetric stretching) mode around 5 μm is by far the strongest feature. Its profile in both the amorphous and crystalline forms is highly asymmetric and distinctly broad, which has been suggested to be caused by the isotopic shifts of and disruption of molecular coupling in the matrix by $OC^{33}S$ and $OC^{34}S$ (Verderame & Nixon 1966). The other fundamental features, the ν_1 (symmetric stretching) and ν_2 (bending) modes, are significantly weaker than the ν_3 mode in both the amorphous and crystalline ices. Several very weak combination and overtone bands are also present in the investigated spectral range. The peak positions of all of the assigned modes are provided in Table 5.2. A small peak at 2340 cm^{-1}, assigned to CO_2, indicates a minor degree of atmospheric contamination. Using the band strength of the asymmetric stretching mode of pure amorphous CO_2 (Gerakines & Hudson

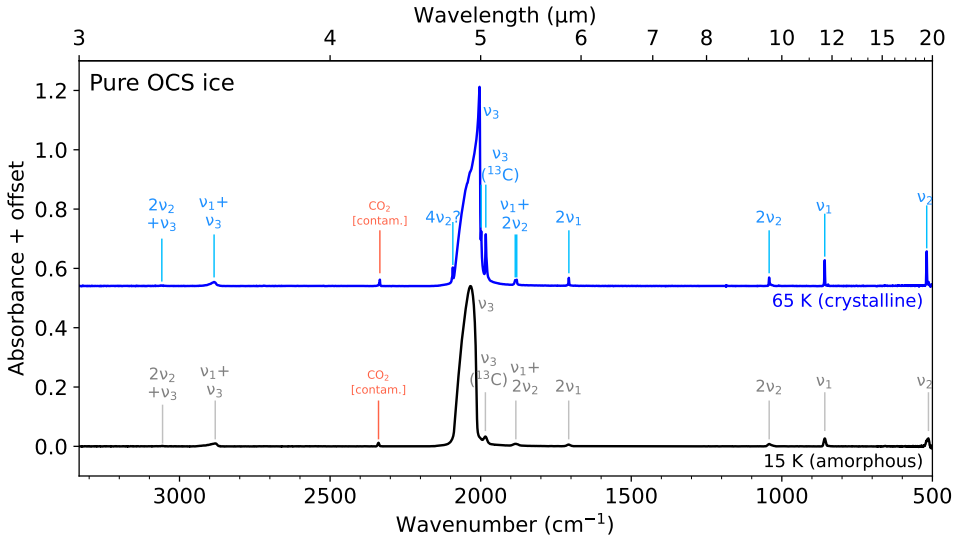

Figure 5.1: Infrared spectra of amorphous (black trace) and crystalline (blue trace) pure OCS ice measured at 15 and 65 K, respectively. Both ices were deposited at 15 K; the crystalline ice was heated from 15 K to 65 K at a rate of 25 K hr^{-1}. Assignments to the absorption features are labeled, and peak positions of these features are provided in Table 5.2. A small feature ∼2340 cm^{-1} assigned to CO_2 ice indicates minor atmospheric contamination.

Table 5.2: Positions and assignments of IR absorption features in pure OCS ice spectra measured at 15 K (amorphous) and 65 K (crystalline).

Assignment[a]	Peak position 15 K		Peak position 65 K	
	(cm^{-1})	(μm)	(cm^{-1})	(μm)
$2\nu_2$+ν_3	3056.3	3.272	3058.7	3.269
ν_1+ν_3	2881.4	3.471	2885.2	3.466
CO_2 contam.	2339.2	4.275	2334.7	4.283
$4\nu_2$?	-	-	2092.4	4.779
ν_3 (asymm. str.)	2033.7	4.917	2003.7	4.991
ν_3 ^{18}OCS	-	-	1998.1	5.005
ν_3 O^{13}CS	1984.3	5.040	1982.9	5.043
ν_1+$2\nu_2$[b]	1883.2	5.310	1885.2 1880.2	5.304 5.319
$2\nu_1$	1707.7	5.856	1707.1	5.858
$2\nu_2$	1042.0	9.597	1042.1	9.596
ν_1 (symm. str.)	857.3	11.665	857.5	11.662
ν_2 (bend)	513.1	19.489	518.9	19.272

[a] Based on assignments from Verderame & Nixon (1966).
[b] Feature is split in crystalline spectrum.

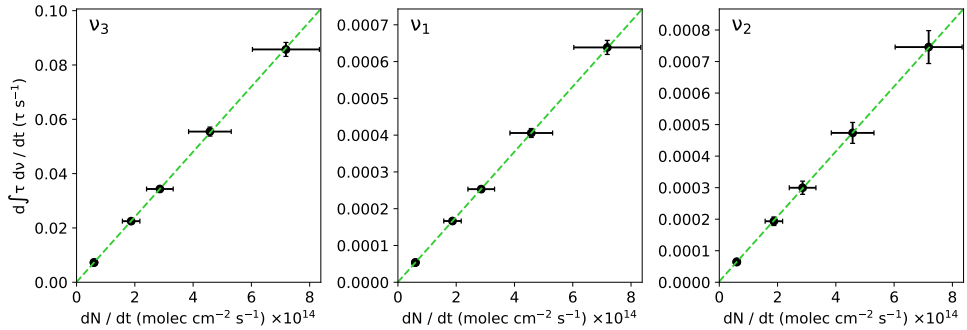

Figure 5.2: Time-derivative Beer's Law plots used to derive the apparent band strengths of the fundamental IR modes of amorphous OCS ice at 15 K. The black points denote the experimental data, with each point representing an individual ice deposition with a given deposition rate in units of column density growth per second, and the dashed green lines denote the best linear fit to the data calculated using the York method.

2015), this contamination is estimated to be on the order of ∼0.2% with respect to OCS. A table containing the peak position, FWHM, and relative integrated absorbance of the ν_3 mode in pure OCS ice throughout its warm-up from 15 to 83 K is provided in the Supporting Information.

The apparent band strengths A' of the three fundamental OCS modes in pure amorphous OCS ice at 15 K were calculated using the method outlined in the Methods section. The resulting A' values are presented in Table 5.3, and the time-derivative Beer's Law plots used to calculate these values are shown in Figure 5.2. Our A' value for the ν_3 mode, 1.20×10^{-16} cm molec^{-1}, is exactly consistent with that reported for pure amorphous OCS ice at 10 K by Yarnall & Hudson 2022. However, we note that our chosen integration range for this peak differs from that listed in Table 2 in Yarnall & Hudson 2022, 2154-2070 cm^{-1}, because their range excludes a majority of the absorption of this feature, leading us to conclude it likely includes a typo.

Our measured A' values of the OCS ν_1 and ν_2 modes are both over two orders of magnitude lower than that of the ν_3 mode. Given such low A' values in combination with the relatively low abundance of OCS in interstellar ices as determined from the ν_3 mode, we conclude that these bands are not likely to be practical in future observational studies and therefore exclude them from the analysis of the OCS ice mixtures.

5.3.2 OCS ice mixtures

The profiles of the OCS ν_3 features at select temperatures in all of the ice mixtures investigated in this work are presented in Figure 5.3. In Figure 5.4, the extracted peak positions and FWHMs of the OCS ν_3 features from these experiments are overplotted with the peak positions and FWHMs extracted from Gaussian fits to the 4.9 μm feature observed toward massive protostars (or massive young stellar objects; MYSOs) by Boogert et al. 2022. (The binary OCS:CO mixtures and the OCS:CO:H_2S 1:20:1 mixtures are excluded from this fig-

Table 5.3: Band strengths of the fundamental vibrational modes of OCS ice, both pure and in mixtures with CH_3OH and CO in the case of the ν_3 mode, at 15 K.

Feature	Ice	Ratio	Peak position (cm^{-1})	Peak position (μm)	A' (cm $molec^{-1}$)	Integration range (cm^{-1})
ν_3	OCS	-	2033.7	4.917	$1.20(\pm0.12)\times10^{-16}$	2197-1909
	$OCS:CH_3OH$	1:20	2041.5	4.898	$1.21(\pm0.13)\times10^{-16}$	2106-1999
	$OCS:CH_3OH$	1:40	2041.5	4.898	$1.18(\pm0.13)\times10^{-16}$	2106-1999
	$OCS:CO:CH_3OH$	1:20:20	2040.8	4.900	$1.19(\pm0.13)\times10^{-16}$	2078-1999
	$OCS:CO:CH_3OH$	1:40:20	2041.3	4.899	$1.20(\pm0.13)\times10^{-16}$	2078-1999
	$OCS:CO:CH_3OH$	1:20:10	2041.2	4.899	$1.21(\pm0.13)\times10^{-16}$	2078-1999
	$OCS:CO:CH_3OH$	1:40:10	2044.7	4.891	$1.24(\pm0.13)\times10^{-16}$	2078-1999
ν_1	OCS	-	857.2	11.67	$8.86(\pm0.91)\times10^{-19}$	867-839
ν_2	OCS	-	514.2	19.45	$1.03(\pm0.11)\times10^{-18}$	530.5-505.8

ure due to their poor fits to the observations and substructures with multiple peaks.) Tables containing the peak positions, FWHMs, and relative integrated absorbances of the OCS ν_3 mode in these ice mixtures throughout their warm-up from 15 to 100 K are provided in the Supporting Information.

OCS:CH_3OH ice mixtures

In all of the binary OCS:CH_3OH mixtures, the OCS peak profile is symmetric and Gaussian-like, and its position is sensitive to temperature: it lies around ∼2041.5 cm^{-1} (4.898 μm) at 15 K and gradually blueshifts with increasing temperature to ∼2042.7 cm^{-1} (4.895 μm) at 100 K in all of the investigated OCS:CH_3OH mixing ratios. The FWHM, on the other hand, is sensitive to both temperature and the OCS:CH_3OH ratio. For example, the FWHM decreases from ∼23 to ∼19 cm^{-1} when the OCS:CH_3OH concentration decreases from 1:10 to 1:20 at 15 K, but a similar decrease in the FWHM also occurs during the warm-up of the OCS:CH_3OH 1:10 mixture. However, differences between the FWHMs of the OCS:CH_3OH 1:20 and 1:40 mixtures are much smaller. Based on this trend, we expect that increasing the dilution factor of OCS:CH_3OH beyond 1:40 would have very small effects on the OCS peak profile.

Notably, while several of the peak profiles observed by Boogert et al. 2022 can be well fit with our OCS:CH_3OH mixtures, many other observed peak positions are too redshifted (by 0.001-0.01 μm) to be sufficiently fit with them.

Given the similarity of these spectra to some of the observations, we derived apparent band strengths of the OCS ν_3 band in the OCS:CH_3OH 1:20 and 1:40 mixtures using the procedure described in the Methods section and report these values in Table 5.3. Within our uncertainties, these A' values are consistent with the A' value of pure OCS.

OCS:CO ice mixtures

Mixing OCS with CO results in an OCS peak blueshift of ∼5-10 cm^{-1} with respect to the OCS peak positions in the OCS:CH_3OH mixtures. Such a peak position is too blueshifted to fit observations. Furthermore, at the higher dilution factors (OCS:CO 1:20 and 1:40), the OCS feature splits into four blended but distinct peaks (see Figure 5.3). Similar splitting is observed in OCS:Ar and OCS:N_2 1:200 mixtures, where it has been attributed to isolated and aggregated OCS molecules within the Ar or N_2 matrices (Verderame & Nixon 1966), as the multiple peaks eventually disappear at even higher dilution factors. These split peak profiles do not match the observed Gaussian-like profile of interstellar OCS ice. Between 30-40 K, the multi-peak structures transform into very broad, asymmetric features similar to the peak structure of pure OCS ice because the CO ice desorbs between these temperatures, effectively distilling the ice and leaving behind nearly pure solid OCS.

OCS:CO:CH_3OH mixtures

Most of the investigated tertiary OCS:CO:CH_3OH mixtures have similar OCS profiles to the OCS:CH_3OH mixtures, but with two notable differences. First, the profiles of the OCS:CO:CH_3OH mixtures are slightly asymmetric at lower temperatures. The effect is most pronounced at 15 K and in the mixtures with the lowest CH_3OH concentrations (e.g., see the OCS:CO:CH_3OH 1:20:2 peak in Figure 5.3) but is still observed in the spectra up to ∼40

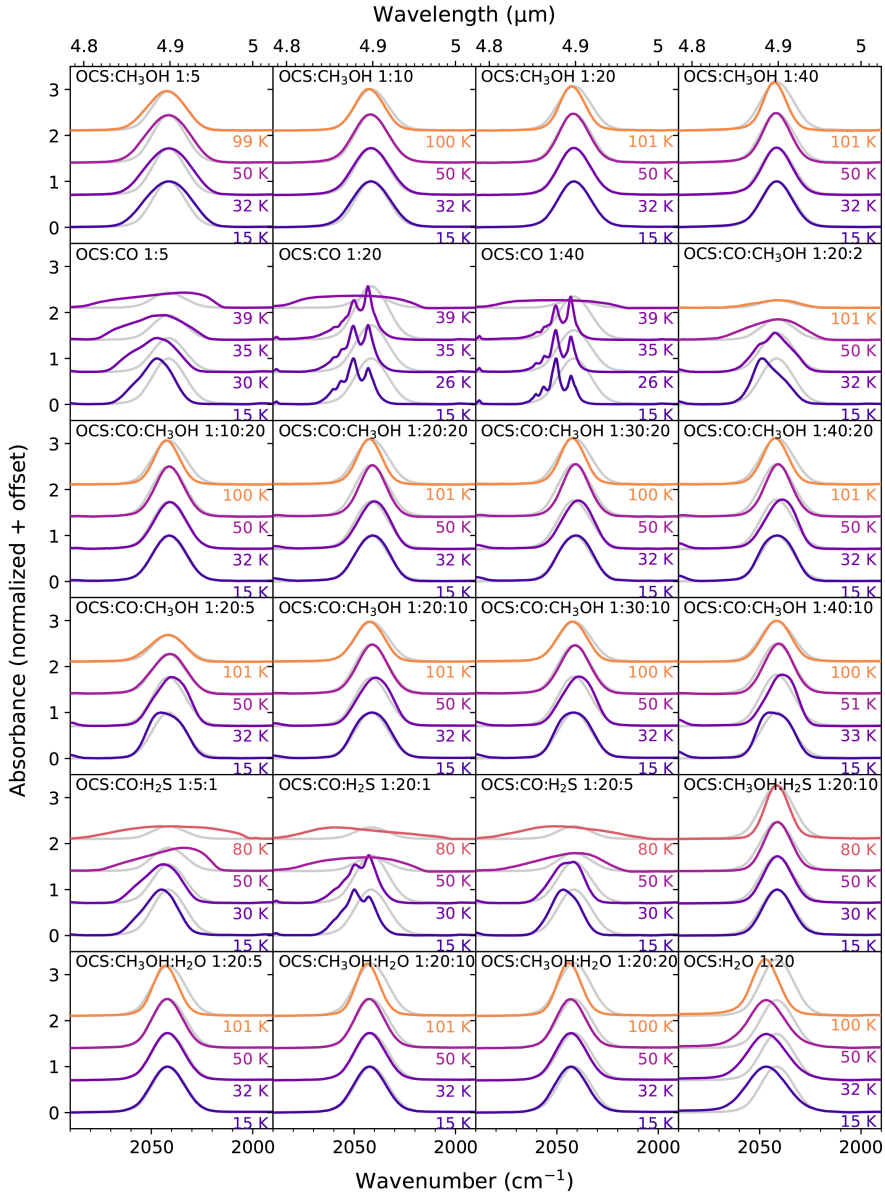

Figure 5.3: OCS ν_3 bands at select temperatures in all investigated binary and tertiary OCS-containing ice mixtures. All of the spectra are normalized so that the peak absorbance of the ν_3 mode at 15 K is equal to 1 in each set of spectra from a given mixture. The profile of the OCS ν_3 mode in the OCS:CH_3OH 1:20 ice mixture at 15 K is scaled to and plotted with all of the peaks (in gray) to facilitate comparisons of peak positions and profiles between the different mixtures.

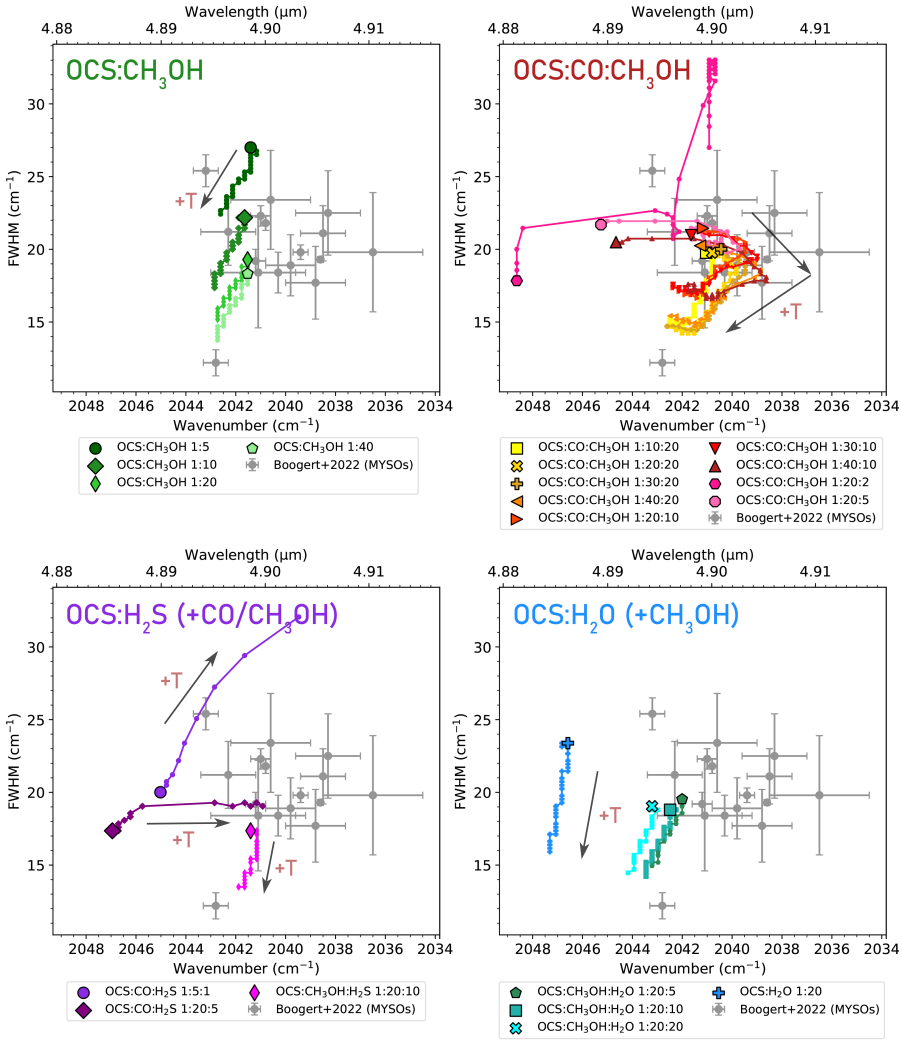

Figure 5.4: Peak positions and FWHMs of the OCS ν_3 mode in all of the investigated laboratory mixtures (color), excluding the binary OCS:CO mixtures and the OCS:CO:H_2S 1:20:1 mixture. The large outlined symbols denote mixtures at 15 K, while the traces and smaller symbols denote how the peak profile changes with increasing temperature. The black arrows indicate the direction of temperature increase. All mixtures are plotted up to 100 K except the OCS:CO:H_2S mixtures, which are only plotted up to 37 K because above this temperature, the OCS ν_3 feature in these mixtures becomes significantly broader than the peak in observations. The peak positions and FWHMs of the Gaussian profiles fit to the 4.9 μm band observed toward massive young stellar objects (MYSOs) by Boogert et al. 2022 are plotted in gray.

K, before a significant portion of the deposited CO begins to desorb. Second, the OCS peak positions in these mixtures tend to be slightly blueshifted relative to the OCS:CH_3OH mixtures at 15 K, but as the temperatures increase to ∼30-35 K, the peaks shift toward longer wavelengths. In the OCS:CO:CH_3OH 1:40:10 mixture, a maximum redshift is achieved at 35 K, with a peak position of 2038.6 cm^{-1} (4.905 μm). Such redshifted profiles provide substantially better fits to many of the redshifted observations.

It is important to note that these experiments demonstrate how even a small concentration of CH_3OH in the matrix has a pronounced effect on the OCS peak profile – i.e., the mixture does not have to be CH_3OH-dominated for the OCS peak to have a profile similar to that in the OCS:CH_3OH mixtures. For example, in the CO-dominated OCS:CO:CH_3OH 1:20:5 mixture, the OCS peak profile looks much more similar to the peak in the OCS:CH_3OH 1:5 mixture than in the OCS:CO 1:20 mixture (see Figure 5.3).

Given the match in redshifted peak position of several of the OCS:CO:CH_3OH mixtures to the MYSO observations in Boogert et al., we calculated the apparent band strengths of the OCS ν_3 mode in the 1:20:20, 1:40:20, 1:20:10, and 1:40:10 mixtures using the procedure outlined in the Methods section and report these values in Table 5.3. As was the case for the OCS:CH_3OH mixtures, these A' values are consistent with the A' value of pure OCS within our reported uncertainties.

OCS:CO:H_2S and OCS:CH_3OH:H_2S mixtures

The three investigated tertiary OCS:CO:H_2S mixtures have significantly blueshifted and markedly asymmetric OCS peaks at 15 K. As they are heated to 30-40 K, their peaks redshift toward the observed values but remain quite asymmetric, making them poor fits to the observations despite the apparent experimental overlap with the observational data in Figure 5.4. At higher temperatures, much of the deposited CO desorbs, and the OCS peaks become much broader than the observations as the OCS ice is effectively distilled. Further OCS distillation occurs in these mixtures between 70-80 K when H_2S desorbs.

The OCS peak profile of the OCS:CH_3OH:H_2S 1:20:10 mixture is nearly identical to that of the most dilute OCS:CH_3OH mixtures. Therefore, the OCS peak profile is not sensitive to the presence of H_2S in CH_3OH-dominated matrices.

OCS:H_2O and OCS:CH_3OH:H_2O mixtures

The OCS profile in the investigated H_2O-containing mixtures is symmetric and Gaussian-like, similar to the binary CH_3OH mixtures. The binary OCS:H_2O 1:20 mixture is far too blueshifted (by at least ∼5 cm^{-1}) to fit any of the observations, as noted previously by Palumbo et al. 1995. However, the tertiary mixtures of OCS:CH_3OH:H_2O explored here, even those with equivalent concentrations of CH_3OH and H_2O like the 1:20:20 mixture, have OCS peak profiles and positions that are very similar to those of the binary OCS:CH_3OH mixtures. They are also slightly blueshifted, but not by enough to lie outside of the observed OCS peak profile range considering errors. These results demonstrate again that the presence of CH_3OH in the ice matrix has a strong effect on the OCS peak profile, even if it is not the only dominant matrix species.

5.4 Astronomical implications

With the spectra collected in this work, we show that many of the observed OCS ν_3 peak positions that were too redshifted to be fit with any previously available nonirradiated laboratory ice mixtures can now actually be fit quite well with tertiary OCS:CO:CH_3OH mixtures. In the bottom two panels of Figure 5.5, we demonstrate how OCS:CO:CH_3OH mixtures provide good fits to the OCS ice features observed toward W33A and G029.8620-00.0444 (hereafter G029.8620), two embedded massive protostars (Boogert et al. 2022) observed via the NASA InfraRed Telescope Facility (IRTF). The massive protostar G029.8620 in particular has the highest quality OCS feature of the IRTF sample, and it is shifted significantly to longer wavelengths with respect to binary OCS:CH_3OH mixtures. This is the case even after the correction for a Doppler velocity shift of +100 km s^{-1} with respect to the Local Standard of Rest (Areal et al. 2020) and the motion of the Earth around the Sun at the date of the IRTF observations (this correction was not applied in Boogert et al. 2022).
These laboratory spectra therefore provide an alternative explanation to that presented by Boogert et al. 2022 for the observed OCS peak positions – namely, that solid-state interstellar OCS may be intimately mixed with both CO and CH_3OH ice. This result is one of many that supports a close chemical relationship between CO and CH_3OH (Watanabe & Kouchi 2002; Fuchs et al. 2009; Cuppen et al. 2011; Penteado et al. 2015) and is consistent with the hypothesis that CO is a chemical precursor of OCS (Shingledecker et al. 2020). Unfortunately, analysis of more precise physicochemical parameters like the OCS:CO:CH_3OH ratio and temperature of the ice matrix surrounding OCS cannot be reliably determined by analyzing the OCS ν_3 peak profile due to the degenerate effects of mixing ratios and temperatures on both the OCS peak position and FWHM in the OCS:CO:CH_3OH laboratory mixtures.

Conversely, our data do not provide conclusive evidence for OCS mixing with H_2S, another suggested OCS precursor (Ferrante et al. 2008; Santos et al. 2024a), in interstellar ices, although they do not refute the possibility, either. The OCS:CH_3OH:H_2S 1:20:10 mixture demonstrates that the presence of H_2S in a CH_3OH-dominated matrix does not have a strong effect on the OCS peak profile, even at relatively high (10:1) H_2S:OCS ratios. Significantly higher concentrations of H_2S are unlikely given that currently available H_2S ice upper limits in the literature result in H_2S:OCS ratio upper limits of $\lesssim$4 (Jiménez-Escobar & Muñoz Caro 2011; McClure et al. 2023). The asymmetric profiles of the OCS bands in the OCS:CO:H_2S mixtures investigated here do not match the more symmetric profiles of the OCS features reported in irradiated laboratory CO:H_2S ice mixtures (Ferrante et al. 2008; Garozzo et al. 2010), which may be due to the presence of several other irradiation products in the latter ices. It is possible that including CH_3OH in the nonirradiated OCS:CO:H_2S mixtures could result in more symmetric OCS features that would better match observations, but any changes in the OCS peak profile due to H_2S in such mixtures are likely to be small (given the tight constraints on H_2S ice abundances from the current upper limits) and perhaps also degenerate with other physicochemical effects.

Finally, we include in Figure 5.5 one of the first observations of OCS ice toward a dense core in front of a background star, J110621 McClure et al. (2023), observed by the *James Webb* Space Telescope (JWST). Although the feature is contaminated by CO gas absorption lines from the photosphere of the background star, a peak profile can be roughly extracted by fitting to the data points between the absorption lines, resulting in an extracted peak position that is blueshifted relative to the OCS:CH_3OH 1:20 position. The laboratory data from this

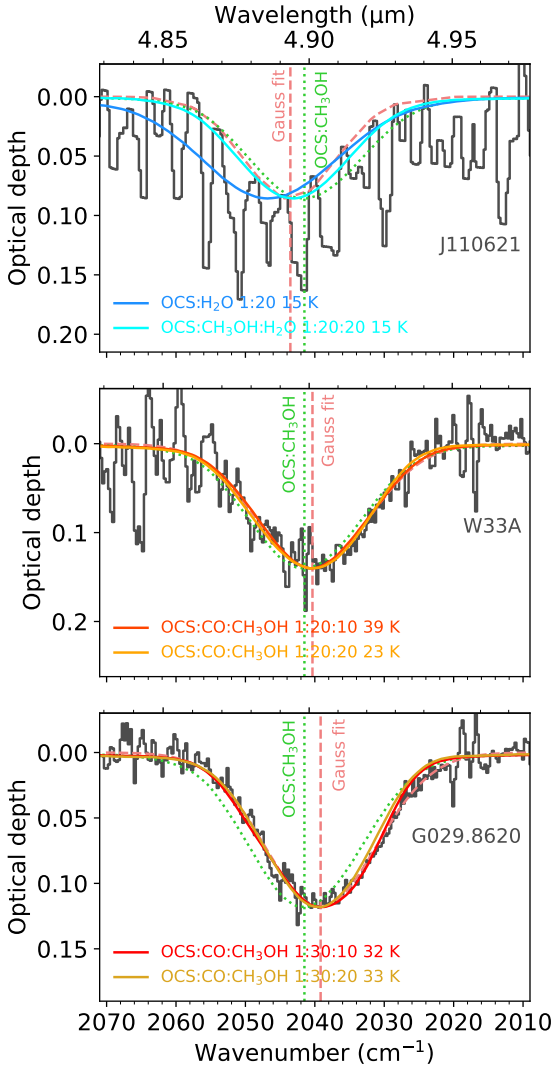

Figure 5.5: OCS ν_3 mode observed toward three icy sightlines (gray traces) overplotted with select laboratory OCS ice mixtures from this work (colored traces). A Gaussian fit to each observed feature (dashed coral trace) and the laboratory OCS:CH_3OH 1:20 15 K spectrum (dotted green trace), along with vertical lines marking their respective peak positions, are also overplotted to serve as points of reference and to facilitate visual comparisons between the different sources and laboratory data. The observational data include the dense core in front of a background star J110621 (top, McClure et al. 2023), the massive protostar W33A (middle, Boogert et al. 2022), and the massive protostar G029.8620 (bottom, Boogert et al. 2022). CO gas lines were removed from the MYSO spectra (see Boogert et al. 2022).

work that provides the best match to such a profile is the OCS:CH_3OH:H_2O 1:20:20 mixture. In their analysis of this source, McClure et al. 2023 found that the local cloud density may still be too low to support catastrophic CO freezeout, and that some portion of the detected CH_3OH ice may be mixed with H_2O, possibly due to early CH_3OH formation via a pathway like CH_4+OH in a H_2O-rich environment (Qasim et al. 2018). The blueshift in the OCS peak position toward this source could be considered evidence for early formation of both OCS and CH_3OH in a more H_2O-rich ice phase, although this evidence remains very tenuous given that the overlapping photospheric contamination may create distortions in the observed OCS profile, leading to higher uncertainties in the extracted peak position.

Given the spectroscopic degeneracies, we do not claim that our laboratory spectra provide unique fits to the OCS ice observations. Therefore, our fits do not strictly preclude other chemical environments, like those investigated by Ferrante et al. 2008 and Garozzo et al. 2010, providing equally satisfactory fits. Our fits do, however, provide evidence supporting plausible chemical environments of OCS ice comprising only simple ice species that are securely and abundantly observed in dense star-forming regions.

5.5 Conclusions

This work provides the astrochemical community with a library of new laboratory IR transmission spectra of OCS-containing ice mixtures to aid analysis of observations of OCS interstellar ices. Apparent band strengths, peak positions, and FWHMs of the OCS asymmetric stretching mode (ν_3) in these mixtures are reported. The main conclusions from this work can be summarized as follows:

- Tertiary laboratory mixtures of OCS:CO:CH_3OH provide the best fits to most of the OCS ice bands currently observed toward the ice envelopes of massive protostars, supporting the previously hypothesized link between these species. The match also supports the late OCS formation scenario, in which most of the observed OCS ice forms in the densest, coldest regions of ice clouds and envelopes where CO freezeout occurs.

- CH_3OH has a strong effect on the profile of the OCS band even when it is not the dominant ice component, and OCS features observed toward several massive protostars can be fit well with OCS:CO:CH_3OH laboratory ice mixtures whose dominant component is CO rather than CH_3OH.

- Specific conclusions regarding local OCS concentration or OCS ice temperature based on the OCS peak profile are hindered by the degenerate effects of these parameters. Taking into account previous work, this degeneracy also applies to proton-irradiated ices containing H_2S, CO, and H_2O (Ferrante et al. 2008).

- The apparent band strength of OCS in OCS:CH_3OH and OCS:CO:CH_3OH mixtures is consistent with that of pure OCS ice within our reported uncertainties. We recommend that a value of 1.2×10^{-16} cm molec^{-1} is used to calculate OCS column densities in interstellar ices.

- Our data neither support nor refute possible chemical links between H_2S and OCS, as the OCS:CO:H_2S mixtures collected as part of this work have asymmetric OCS profiles

that do not match any observations, but the investigated OCS:CH_3OH:H_2S mixture has a similar profile to binary OCS:CH_3OH mixtures that fit some of the observed OCS peaks well.

- While OCS:H_2O mixtures are too blueshifted to fit any current OCS observations, OCS:CH_3OH:H_2O mixtures may provide a good fit to an OCS feature observed toward a background star behind a dense cloud, suggesting that some OCS may form earlier in a phase of the ice that is still relatively H_2O-rich. However, this conclusion remains tenuous due to spectral contamination by photospheric CO gas absorptions complicating the OCS profile extraction toward this source.
- Given the weak apparent band strengths of the OCS symmetric stretching (ν_1) and bending (ν_2) modes and the relatively low abundance of OCS ice in dense star-forming regions, the very strong OCS asymmetric stretching (ν_3) mode remains the only likely detectable feature of this molecule in interstellar ices in the near future.

These laboratory spectra are made available for public use and enjoyment on the Leiden Ice Database (LIDA, (Rocha et al. 2022)).

5.6 Acknowledgements

This paper is dedicated to the memory of the late Harold Linnartz, who provided indispensable scientific guidance and inspiration throughout the collection and analysis of this data. K.S. thanks Ewine van Dishoeck for helpful scientific discussions, Julia Santos for experimental support, and Martijn Witlox and Robin Schrama for mechanical support. K.-J.C. is grateful for support from the Dutch Research Council (NWO) via the Veni fellowship. Astrochemistry at Leiden is supported by funding from the European Research Council (ERC) under the European Union's Horizon 2020 research and innovation programme (grant agreement No. 101019751 MOLDISK), the Netherlands Research School for Astronomy (NOVA), and the Danish National Research Foundation through the Center of Excellence "InterCat" (Grant agreement no.: DNRF150).

5.A Supplemental Information

5.A.1 OCS ν_3 peak positions, FWHMs, and relative integrated absorbances

This appendix presents the peak positions, FWHMs, and relative integrated absorbances (with respect to the integrated absorbance of each mixture at 15 K) of the OCS ν_3 feature in all OCS-bearing ice mixtures investigated in this work. The uncertainty of the peak positions and FWHMs is 0.5 cm^{-1}.

Table 5.A.4: Peak positions, FWHMs, and relative integrated absorbances (with respect to the integrated absorbance of each mixture at 15 K) of the OCS $\nu 3$ feature in pure and binary OCS ices at various temperatures.

Matrix	T	Peak		FWHM		Rel. integ. abs.
	(K)	cm^{-1}	μm	cm^{-1}	μm	(w.r.t. 15 K)
OCS*	15	2034.1	4.916	55.9	0.134	1.00
	50	2029.7	4.927	53.5	0.128	1.03
	65	2003.7	4.991	46.3	0.113	1.07
	83	2003.4	4.991	27.5	0.068	1.13
OCS:CH_3OH 1:5	15	2041.4	4.899	27.0	0.065	1.00
	52	2041.6	4.898	25.3	0.061	0.99
	66	2042.1	4.897	24.3	0.058	0.98
	80	2042.4	4.896	23.6	0.057	0.97
	95	2042.6	4.896	22.7	0.054	0.85
OCS:CH_3OH 1:10	15	2041.6	4.898	22.2	0.053	1.00
	50	2042.1	4.897	20.5	0.049	0.99
	60	2042.4	4.896	19.8	0.047	0.98
	71	2042.6	4.896	19.0	0.046	0.98
	81	2042.8	4.895	18.3	0.044	0.97
	99	2042.8	4.895	17.4	0.042	0.76
OCS:CH_3OH 1:20	15	2041.5	4.898	19.3	0.046	1.00
	48	2042	4.897	17.8	0.043	1.00
	59	2042.2	4.897	17.4	0.042	0.99
	69	2042.5	4.896	16.6	0.040	0.99
	80	2042.7	4.895	15.9	0.038	0.98
	99	2042.7	4.895	15.2	0.036	0.82
OCS:CH_3OH 1:40	15	2041.5	4.898	18.3	0.044	1.00
	48	2042	4.897	16.6	0.040	1.00
	60	2042.2	4.897	16.2	0.039	0.99
	71	2042.5	4.896	15.4	0.037	0.98
	81	2042.7	4.895	14.7	0.035	0.97
	99	2042.7	4.895	13.7	0.033	0.85
OCS:CO 1:5*	15	2047.3	4.884	19.8	0.047	1.00
	32	2047.6	4.884	30.1	0.072	0.92
	35	2043.7	4.893	35.7	0.085	0.90
OCS:CO 1:20*	15	2050.2	4.878	14.0	0.033	1.00
	26	2043.2	4.894	14.7	0.035	1.01
	30	2043.2	4.894	12.8	0.030	1.02
	35	2043.2	4.894	12.3	0.029	1.03
OCS:CO 1:40*	15	2050.7	4.876	5.3	0.013	1.00
	31	2043	4.895	5.1	0.012	1.00
	35	2043	4.895	4.8	0.012	0.97

* indicates that the OCS ν_3 mode in the marked ice has a strongly asymmetric or split (i.e., non-Gaussian) peak profile.

Table 5.A.5: Peak positions, FWHMs, and relative integrated absorbances (with respect to the integrated absorbance of each mixture at 15 K) of the OCS $\nu 3$ feature in select tertiary OCS:CO:CH_3OH mixtures at various temperatures.

Matrix	T (K)	Peak cm^{-1}	Peak μm	FWHM cm^{-1}	FWHM μm	Rel. integ. abs. (w.r.t. 15 K)
OCS:CO:CH_3OH 1:20:2*	15	2048.6	4.881	17.8	0.043	1.00
	25	2043.1	4.895	22.7	0.054	0.98
	41	2041.2	4.899	29.9	0.072	0.79
	50	2040.9	4.900	31.8	0.076	0.78
	71	2040.9	4.800	32.3	0.077	0.78
	90	2040.9	4.900	31.6	0.076	0.52
OCS:CO:CH_3OH 1:10:20	15	2041	4.899	19.8	0.047	1.00
	36	2040.8	4.900	18.6	0.045	1.00
	50	2041.3	4.899	17.1	0.041	0.98
	60	2041.5	4.898	15.9	0.038	0.98
	70	2041.8	4.898	15.2	0.036	0.98
	84	2042.2	4.897	14.7	0.035	0.97
	94	2042.5	4.896	15.2	0.036	0.90
OCS:CO:CH_3OH 1:20:20	15	2040.8	4.900	19.8	0.047	1.00
	33	2039.8	4.902	18.3	0.044	0.99
	47	2040.8	4.900	16.2	0.039	0.95
	60	2041.3	4.899	14.7	0.035	0.94
	72	2041.8	4.898	14.5	0.035	0.93
	90	2042.5	4.896	14.7	0.035	0.93
OCS:CO:CH_3OH 1:30:20	15	2040.4	4.901	20.0	0.048	1.00
	32	2039.5	4.903	18.6	0.045	1.00
	42	2040.4	4.901	16.6	0.040	0.97
	51	2040.9	4.900	15.7	0.038	0.96
	59	2041.2	4.899	14.9	0.036	0.96
	65	2041.4	4.899	14.5	0.035	0.96
	72	2041.6	4.898	14.5	0.035	0.95
	83	2042.1	4.897	14.7	0.035	0.94
	93	2042.6	4.896	14.7	0.035	0.89
OCS:CO:CH_3OH 1:40:20	15	2041.3	4.899	20.2	0.049	1.00
	22	2040.6	4.901	20.2	0.049	1.01
	32	2038.9	4.905	18.6	0.045	1.02
	41	2040.6	4.901	16.6	0.040	0.95
	50	2040.8	4.900	15.9	0.038	0.95
	60	2041.3	4.899	15.2	0.036	0.95
	71	2041.5	4.898	14.9	0.036	0.95
	80	2041.8	4.897	15.2	0.036	0.93
	90	2042.2	4.897	15.2	0.036	0.93
	99	2042.5	4.896	15.4	0.037	0.86

* indicates that the OCS ν_3 mode in the marked ice has a strongly asymmetric or split (i.e., non-Gaussian) peak profile.

Table 5.A.6: Peak positions, FWHMs, and relative integrated absorbances (with respect to the integrated absorbance of each mixture at 15 K) of the OCS $\nu 3$ feature in select tertiary OCS:CO:CH_3OH mixtures at various temperatures.

Matrix	T (K)	Peak cm^{-1}	Peak μm	FWHM cm^{-1}	FWHM μm	Rel. integ. abs. (w.r.t. 15 K)
OCS:CO:CH_3OH 1:20:5	15	2045.3	4.889	21.7	0.052	1.00
	22	2043.1	4.895	21.9	0.053	1.00
	35	2039.7	4.903	20.0	0.048	1.01
	50	2040.7	4.900	20.2	0.049	0.85
	60	2040.7	4.900	20.0	0.048	0.84
	71	2040.9	4.900	20.2	0.049	0.83
	80	2041.2	4.899	20.5	0.049	0.83
	90	2041.4	4.899	21.5	0.051	0.78
	96	2041.6	4.898	21.2	0.051	0.68
OCS:CO:CH_3OH 1:20:10	15	2041.2	4.899	21.5	0.051	1.00
	20	2040.7	4.900	21.2	0.051	1.00
	30	2039.5	4.903	20.0	0.048	1.00
	38	2040.2	4.901	19.0	0.046	0.95
	45	2040.7	4.900	18.3	0.044	0.94
	56	2041.2	4.899	17.1	0.041	0.93
	65	2041.4	4.899	16.9	0.040	0.93
	75	2041.6	4.898	16.9	0.040	0.92
	86	2042.1	4.897	17.4	0.042	0.90
	95	2042.4	4.896	17.4	0.042	0.82
OCS:CO:CH_3OH 1:30:10	15	2041.6	4.898	21.0	0.050	1.00
	21	2040.4	4.901	21.0	0.050	1.00
	32	2039	4.904	19.3	0.046	1.00
	44	2040.7	4.900	18.3	0.044	0.93
	56	2041.2	4.899	17.4	0.042	0.92
	66	2041.4	4.899	17.1	0.041	0.92
	75	2041.6	4.898	17.1	0.041	0.91
	86	2042.1	4.897	17.4	0.041	0.90
	95	2042.4	4.896	17.6	0.042	0.83
OCS:CO:CH_3OH 1:40:10	15	2044.7	4.891	20.5	0.049	1.00
	22	2040.3	4.901	20.2	0.049	1.01
	31	2038.6	4.905	18.1	0.043	1.01
	40	2040.3	4.901	16.9	0.041	0.92
	51	2040.6	4.901	16.9	0.041	0.93
	61	2040.6	4.901	16.6	0.040	0.93
	72	2040.8	4.900	16.6	0.040	0.93
	84	2041.3	4.899	17.1	0.041	0.92
	95	2041.8	4.898	17.1	0.041	0.83

* indicates that the OCS ν_3 mode in the marked ice has a strongly asymmetric or split (i.e., non-Gaussian) peak profile.

Table 5.A.7: Peak positions, FWHMs, and relative integrated absorbances (with respect to the integrated absorbance of each mixture at 15 K) of the OCS $\nu 3$ feature in tertiary H_2S-containing mixtures at various temperatures.

Matrix	T	Peak		FWHM		Rel. integ. abs.
	(K)	cm^{-1}	μm	cm^{-1}	μm	(w.r.t. 15 K)
OCS:CO:H_2S 1:5:1*	15	2045	4.890	20.0	0.048	1.00
	27	2044.5	4.891	21.2	0.051	0.98
	33	2042.8	4.895	27.2	0.065	0.92
	38	2037.1	4.909	34.0	0.082	0.89
	48	2034.2	4.916	36.4	0.087	0.90
	57	2030.8	4.924	44.4	0.107	0.85
OCS:CO:H_2S 1:20:1*	15	2050	4.880	18.3	0.044	1.00
	24	2040	4.900	18.6	0.044	1.01
	38	2040	4.900	16.4	0.039	0.93
	44	2040	4.900	47.7	0.114	0.80
	51	2040	4.890	50.9	0.121	0.78
	57	2040	4.900	57.6	0.137	0.79
OCS:CO:H_2S 1:20:5*	15	2046.9	4.885	17.4	0.041	1.00
	29	2042.8	4.895	19.3	0.046	1.00
	37	2040.9	4.900	19.0	0.046	0.98
	42	2040	4.902	29.7	0.071	0.82
	51	2040	4.902	39.1	0.093	0.81
	59	2040	4.902	52.6	0.125	0.82
OCS:CH_3OH:H_2S 1:20:10	15	2041.4	4.899	17.4	0.042	1.00
	50	2041.2	4.899	16.2	0.039	0.99
	60	2041.4	4.899	15.4	0.037	0.99
	80	2041.6	4.898	14.5	0.035	0.98
	96	2041.9	4.897	13.5	0.032	0.86

* indicates that the OCS ν_3 mode in the marked ice has a strongly asymmetric or split (i.e., non-Gaussian) peak profile.

Table 5.A.8: Peak positions, FWHMs, and relative integrated absorbances (with respect to the integrated absorbance of each mixture at 15 K) of the OCS $\nu 3$ feature in tertiary H_2S-containing mixtures at various temperatures.

Matrix	T	Peak		FWHM		Rel. integ. abs.
	(K)	cm^{-1}	μm	cm^{-1}	μm	(w.r.t. 15 K)
OCS:CH_3OH:H_2O 1:20:5	15	2042	4.897	19.5	0.047	1.00
	50	2042.2	4.897	18.1	0.043	0.99
	60	2042.5	4.896	17.4	0.042	0.98
	72	2042.7	4.895	16.9	0.040	0.97
	86	2043	4.895	15.9	0.038	0.96
	101	2043.2	4.894	14.9	0.036	0.85
OCS:CH_3OH:H_2O 1:20:10	15	2042.5	4.896	18.8	0.045	1.00
	50	2042.7	4.895	17.4	0.042	0.99
	65	2043	4.895	16.4	0.039	0.98
	75	2043.2	4.894	15.9	0.038	0.97
	87	2043.5	4.894	15.2	0.036	0.95
	101	2043.5	4.894	14.2	0.034	0.87
OCS:CH_3OH:H_2O 1:20:20	15	2043.2	4.894	19.0	0.046	1.00
	50	2043.2	4.894	17.6	0.042	0.99
	60	2043.5	4.894	17.1	0.041	0.98
	71	2043.7	4.893	16.4	0.039	0.97
	81	2043.9	4.893	15.7	0.038	0.96
	100	2044.2	4.892	14.5	0.035	0.89
OCS:H_2O 1:20	15	2046.6	4.886	23.4	0.056	1.00
	50	2046.8	4.886	21.0	0.050	0.98
	66	2047.1	4.885	19.0	0.045	0.97
	89	2047.3	4.884	17.1	0.041	0.95
	101	2047.3	4.884	15.9	0.038	0.88

* indicates that the OCS ν_3 mode in the marked ice has a strongly asymmetric or split (i.e., non-Gaussian) peak profile.

5.B Bibliography

Aikawa, Y., Kamuro, D., Sakon, I., et al. 2012, A&A, 538, A57
Areal, M. B., Paron, S., Fariña, C., et al. 2020, A&A, 641, A104
Boogert, A., Brewer, K., Brittain, A., & Emerson, K. 2022, ApJ, 941, 32
Boogert, A. A., Gerakines, P. A., & Whittet, D. C. 2015, ARA&A, 53, 541
Bouilloud, M., Fray, N., Bénilan, Y., et al. 2015, MNRAS, 451, 2145
Chen, Y.-J., Juang, K.-J., Nuevo, M., et al. 2014, ApJ, 798, 80
Cuppen, H., Penteado, E., Isokoski, K., van der Marel, N., & Linnartz, H. 2011, MNRAS, 417, 2809
Ferrante, R. F., Moore, M. H., Spiliotis, M. M., & Hudson, R. L. 2008, ApJ, 684, 1210
Fuchs, G., Cuppen, H., Ioppolo, S., et al. 2009, A&A, 505, 629
Garozzo, M., Fulvio, D., Kanuchova, Z., Palumbo, M., & Strazzulla, G. 2010, A&A, 509, A67
Geballe, T., Baas, F., Greenberg, J., & Schutte, W. 1985, A&A, 146, L6
Gerakines, P. A. & Hudson, R. L. 2015, ApJL, 808, L40
Gibb, E., Whittet, D., Boogert, A., & Tielens, A. 2004, ApJS, 151, 35
Hudgins, D., Sandford, S., Allamandola, L., & Tielens, A. 1993, ApJS, 86, 713
Hudson, R. L. & Gerakines, P. A. 2018, ApJ, 867, 138
Jiménez-Escobar, A. & Muñoz Caro, G. M. 2011, A&A, 536, A91
Laas, J. C. & Caselli, P. 2019, A&A, 624, A108
Loeffler, M., Moore, M., & Gerakines, P. 2016, ApJ, 827, 98
Luna, R., Millán, C., Domingo, M., Santonja, C., & Satorre, M. Á. 2022, ApJ, 935, 134
Luna, R., Molpeceres, G., Ortigoso, J., et al. 2018, A&A, 617, A116
McClure, M. K., Rocha, W., Pontoppidan, K., et al. 2023, Nat. Astro., 7, 431
Palumbo, M., Geballe, T., & Tielens, A. G. 1997, ApJ, 479, 839
Palumbo, M., Tielens, A., & Tokunaga, A. T. 1995, ApJ, 449
Penteado, E., Boogert, A., Pontoppidan, K., et al. 2015, MNRAS, 454, 531
Qasim, D., Chuang, K.-J., Fedoseev, G., et al. 2018, A&A, 612, A83
Rachid, M., Brunken, N., De Boe, D., et al. 2021, A&A, 653, A116
Rocha, W., Rachid, M., Olsthoorn, B., et al. 2022, A&A, 668, A63
Santos, J. C., Linnartz, H., & Chuang, K.-J. 2024a, A&A, 690, A24
Santos, J. C., van Gelder, M. L., Nazari, P., Ahmadi, A., & van Dishoeck, E. F. 2024b, A&A, 689, A248
Shingledecker, C. N., Lamberts, T., Laas, J. C., et al. 2020, ApJ, 888, 52
Slavicinska, K., Rachid, M. G., Rocha, W. R. M., et al. 2023, A&A, 677, A13
Tyagi, H., Manoj, P., Narang, M., et al. 2025, ApJ, 983, 110
Verderame, F. D. & Nixon, E. R. 1966, JCP, 44, 43
Vidal, T. H. & Wakelam, V. 2018, MNRAS, 474, 5575
Watanabe, N. & Kouchi, A. 2002, ApJ, 571, L173
Yarnall, Y. Y. & Hudson, R. L. 2022, ApJL, 931, L4
York, D. 1966, Can. J. Phys., 44, 1079